Journal of Solid State Chemistry 242 (2016) 86–95

Contents lists available at ScienceDirect

Journal of Solid State Chemistry

journal homepage: www.elsevier.com/locate/jssc

# Structural chemistry and magnetic properties of the perovskite $Sr_3Fe_2TeO_9$

Yawei Tang [a], Emily C. Hunter [a], Peter D. Battle [a,*], Robert Paria Sena [b], Joke Hadermann [b], Maxim Avdeev [c], J.M. Cadogan [d]

[a] Inorganic Chemistry Laboratory, University of Oxford, South Parks Road, Oxford OX1 3QR, UK
[b] EMAT, University of Antwerp, Groenenborgerlaan 171, 2020 Antwerp, Belgium
[c] Bragg Institute, Australian Nuclear Science and Technology Organisation, Lucas Heights, NSW 2234, Australia
[d] School of Physical, Environmental and Mathematical Sciences, UNSW Canberra at the Australian Defence Force Academy, Canberra BC 2610, Australia

ARTICLE INFO

*Article history:*
Received 28 April 2016
Received in revised form
24 June 2016
Accepted 27 June 2016
Available online 29 June 2016

*Keywords:*
Trigonal perovskite
Antiferromagnetic perovskite

ABSTRACT

A polycrystalline sample of perovskite-like $Sr_3Fe_2TeO_9$ has been prepared in a solid-state reaction and studied by a combination of electron microscopy, Mössbauer spectroscopy, magnetometry, X-ray diffraction and neutron diffraction. The majority of the reaction product is shown to be a trigonal phase with a 2:1 ordered arrangement of $Fe^{3+}$ and $Te^{6+}$ cations. However, the sample is prone to nano-twinning and tetragonal domains with a different pattern of cation ordering exist within many crystallites. Antiferromagnetic ordering exists in the trigonal phase at 300 K and $Sr_3Fe_2TeO_9$ is thus the first example of a perovskite with 2:1 trigonal cation ordering to show long-range magnetic order. At 300 K the antiferromagnetic phase coexists with two paramagnetic phases which show spin-glass behaviour below ~80 K.



## 1. Introduction

Oxides with crystal structures related to that of the mineral perovskite are among the most intensely studied compounds in solid-state chemistry because of the wide variety of physical properties they can display [1]. Their electrical behaviour ranges from insulating to superconducting and their magnetic properties show a comparable breadth, ranging from spin-glass behaviour [2] to ferromagnetism [3]. Moreover, pairs of these properties can sometimes be combined and the compound can then be described as multiferroic [4].

The extensive range of properties observed stems largely from the ability of the structure to accommodate a wide range of chemical compositions. This in turn derives from its ability to tolerate a significant strain by undergoing distortions that reduce the symmetry of the structure from the cubic ideal to orthorhombic or lower. The flexibility in composition makes it possible to tune the physical properties chemically. The simplest oxide perovskites can be represented by the formula $ABO_3$ where $A$ is a relatively large cation, usually an alkaline earth or rare earth element, that occupies the twelve-coordinate A site, and $B$ is a smaller cation, usually a transition-metal or p-block element that occupies the octahedrally-coordinated B site. Partial cation substitution at either the A site, the B site or both, leading to the formulae $AA'BB'O_6$ and $A_2A'B_2B'O_9$, is one of the strategies that has been employed in order to induce desirable physical properties [5,6]. Whether the strategy is successful often depends on whether the different cation species on the A and B sites occupy their respective sites in an ordered or disordered manner. An ordered arrangement is usually stabilised when the cations at the site differ significantly in their valence or size. Consequently, B-site ordering is quite common in perovskites whereas A-site ordering is relatively rare.

In this study we have focussed on the compound $Sr_3Fe_2TeO_9$ in which only the B site holds more than one species of cation. In two previous accounts [7,8] this compound has been described as a tetragonal perovskite in which the $Fe^{3+}$ and $Te^{6+}$ cations are partially ordered over the six-coordinate B sites. More specifically, the octahedral sites are divided into two subsets that occur alternately in 3 dimensions throughout the structure in a checkerboard pattern. The two subsets thus have the same multiplicity. Ivanov et al. [8] concluded that one subset, or sublattice, is occupied by $Fe^{3+}$ and $Te^{6+}$ in a ratio of 0.72:0.28 and the Fe:Te ratio at the other site is thus 0.61:0.39, see Fig. 1; the corresponding values reported by Augsburger et al. [7] were 0.9:0.1 and 0.57:0.43. Neutron diffraction data collected by Ivanov et al. suggested that the compound showed long-range magnetic ordering below ~260 K with the atomic moments on the two sublattices aligned antiparallel along [001]. The magnetic moments per $Fe^{3+}$ cation

* Corresponding author.
*E-mail address:* peter.battle@chem.ox.ac.uk (P.D. Battle).

http://dx.doi.org/10.1016/j.jssc.2016.06.024

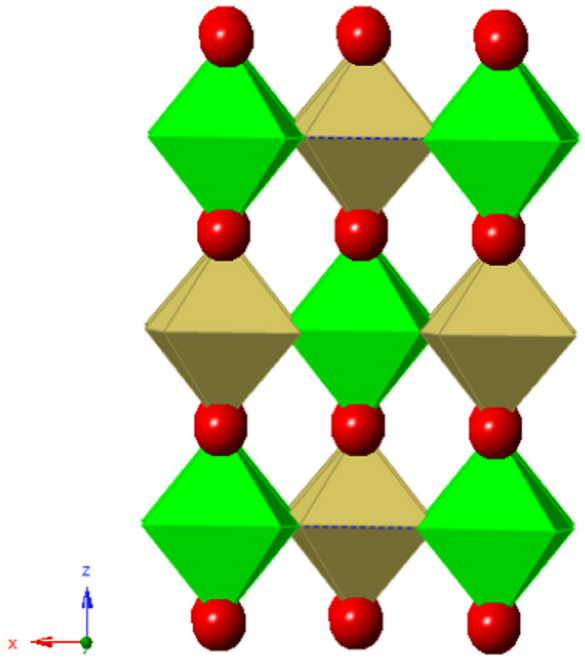


**Fig. 1.** Polyhedral representation of the tetragonal structure proposed for $Sr_3Fe_2TeO_9$ in the space group *I*4/*m*. Red circles represent $Sr^{2+}$ green and khaki octahedra represent sites occupied by a partially ordered distribution of $Fe^{3+}$ and $Te^{6+}$. (For interpretation of the references to color in this figure legend, the reader is referred to the web version of this article).

on the two sites refined to values of ~1.6 and ~1.3 $\mu_B$ at 10 K. These values are very low for a high-spin $d^5$ cation. Furthermore, despite the mismatch in the moments on the two sites, no sharp increase in the magnetisation was seen on cooling the sample below 260 K. However, hysteresis was apparent in the magnetic susceptibility below this temperature. A maximum was observed in the zero-field cooled (ZFC) susceptibility at ~90 K in a measuring field of 100 Oe and at ~60 K in a field of 30 kOe; the susceptibility was field dependent throughout the measured temperature range although, inconsistently, the magnetisation at 300 K was shown to be a linear function of field for $0 < H/kOe < 50$. The field-cooled susceptibility maintained a negative temperature gradient at all temperatures and in all fields. Ivanov et al. suggested that ferrimagnetic ordering is present, at least over short length scales, below 260 K and that the susceptibility maximum observed at low temperature marks the formation of a reentrant spin glass. In contrast, Augsburger et al. reported the onset of ferromagnetism at ~717 K in their sample and they observed a remanent magnetisation 0.35 $\mu_B$ per $Fe^{3+}$ cation at 5 K. They analysed their neutron diffraction data using a model in which nearest-neighbour $Fe^{3+}$ cations were coupled antiferromagnetically and found an ordered moment of ~0.5 $\mu_B$ per $Fe^{3+}$ cation at 300 K and 0.85 $\mu_B$ at 13 K, the latter lower even than the value reported by Ivanov et al. Both of these two studies used samples that were prepared in a solid-state reaction. Djerdi et al. [9] have recently prepared a sample by a sol-gel route. It is reported to adopt the simple cubic perovskite structure with no cation ordering over the B sites and to be ferrimagnetic below 667 K.

The suggestion by Ivanov et al. that the length scale of the magnetic ordering might be important in determining the magnetic properties of $Sr_3Fe_2TeO_9$ is reminiscent of the behaviour of $La_3Ni_2SbO_9$, another $A_3B_2B'O_9$ perovskite, which we have previously described as a relaxor ferromagnet [10,11]. The octahedral sites in this monoclinic compound are divided over two sublattices, as they are in $Sr_3Fe_2TeO_9$. However, in the case of $La_3Ni_2SbO_9$ one sublattice is occupied entirely by $Ni^{2+}$ cations and 2/3 of the second sublattice is occupied by $Sb^{5+}$ with the remaining 1/3 being occupied by $Ni^{2+}$; there is no long-range ordering of the two cation species occupying the second sublattice. The imbalance in the concentration of $Ni^{2+}$ cations on the two sites leads to the observed magnetic behaviour, although local variations in the composition cause the formation of small magnetic domains. Clearly, the net magnetisation is expected to be larger in a compound that contains a more strongly magnetic cation, and it is also likely that the transition temperature will increase above the value of 108 K seen in $La_3Ni_2SbO_9$. Bearing in mind the internal inconsistencies in the description given by Ivanov et al. the differences between the data collected by different authors and the potential of $Sr_3Fe_2TeO_9$ to show enhanced relaxor properties, we have undertaken our own investigation of this compound using a combination of X-ray and neutron diffraction, electron microscopy and Mössbauer spectroscopy. Our results, which differ significantly from those reported previously, are described below.

## 2. Experimental

A polycrystalline sample of $Sr_3Fe_2TeO_9$ was prepared using the standard ceramic method. $SrCO_3$, $Fe_2O_3$ and $TeO_2$ (purity > 99.95%) were weighed out in the appropriate stoichiometric ratio and ground together in an agate mortar for 30 min to give a homogeneous mixture. The mixture was then loaded into an alumina crucible and fired at 700 °C for 24 h. It was then quenched to room temperature, reground and pressed into a pellet that was fired in air at 950 °C for 24 h and subsequently annealed at 1200 °C for 48 h after further grinding. Finally, the furnace was allowed to cool to 800 °C and then the sample was quenched to room temperature.

The black reaction product was initially characterised by X-ray powder diffraction (XRPD) using Cu $K\alpha_1$ radiation. The data, collected at room temperature, were analysed using the Rietveld method as implemented in the GSAS [12] program package. Neutron diffraction data were subsequently collected on the diffractometer Echidna at the Bragg Institute, ANSTO, Australia. The angular region $10 < 2\theta/° < 147.5$ was scanned in steps of 0.05° at temperatures of 300 and 3 K using neutron wavelengths of 1.6215 (5) and 2.4395(5) Å. Data analysis was again performed using the Rietveld method [13]. The peak shape was modelled using the function devised by van Laar and Yelon [14] and the background was fitted using a twelve-term Chebyshev polynomial.

Specimens for electron microscopy were prepared by dispersing crushed $Sr_3Fe_2TeO_9$ powder in ethanol and depositing a few drops of this solution on a copper grid covered with a holey carbon film. Selected area electron diffraction (SAED) patterns were obtained with a Philips CM20 transmission electron microscope, high angle annular dark field scanning transmission electron microscopy (HAADF-STEM) images and atomic resolution energy dispersive X-ray (EDX) maps were acquired with a FEI Titan 80-300 "cubed" microscope equipped with a Super-X detector and operated at 300 kV. Quantitative EDX measurements were also taken of 50 different crystallites on a JEOL 5590 scanning electron microscope.

$^{57}$Fe Mössbauer spectra were collected from a polycrystalline sample of $Sr_3Fe_2TeO_9$ at 295 K and 5 K using a standard transmission spectrometer and a $^{57}$Co**Rh** source. The drive velocity of the spectrometer was calibrated using a 6 μm thick α-Fe foil, at 295 K, and all isomer shifts (δ) are quoted relative to the centre of the α-Fe calibration spectrum. All Mössbauer spectra were fitted using the NORMOS software [15] . Due to the clear asymmetry of the lines associated with the magnetic component, spectra were

also fitted with a distribution of magnetic hyperfine field, using the Le Caër–Dubois software [16].

The magnetic susceptibility of $Sr_3Fe_2TeO_9$ was measured over the temperature range $2 < T/K < 300$ using a Quantum Design MPMS 5000 SQUID magnetometer. Data were collected on warming in a field of 100 Oe after cooling the sample both in the absence of an applied field (zero-field cooled, ZFC) and in the measuring field (field cooled, FC). The isothermal sample magnetisation was measured as a function of field over the range $-50 < H/kOe < 50$ at 300, 150 and 5 K.

## 3. Results

Our preliminary consideration of the XRPD pattern of the product appeared to confirm that $Sr_3Fe_2TeO_9$ adopts a perovskite-like structure. The presence of weak Bragg peaks, most noticeably at angles $2\theta < 30°$, indicated a deviation away from the aristotype cubic perovskite structure, and, influenced by the earlier work of Ivanov et al. [8], we initially indexed and analysed the pattern in the tetragonal space group $I4/m$, with the unit-cell parameters a=5.5749(1), c=7.8963(3) Å, that is $\sim\sqrt{2}a_p \times \sim 2a_p$. Although the fit between the observed and calculated diffraction patterns was good ($R_{wpr}=6.06\%$, $\chi^2=1.47$, see Fig. S1) we noted that some weak reflections, for example at $2\theta=18°$, could not be indexed in the tetragonal cell. These reflections were extremely weak and the fit was very good so we initially assumed that they derived from a minor impurity phase. The results of our electron microscopy study, described below, showed this to be a false assumption.

EDX analysis found a mean Fe:Te ratio of 2.3(3) across the crystallites studied. This value is consistent, within error, with the target composition. SAED patterns, including several tilt series, were taken from many different crystals. All the patterns could be indexed in the trigonal system, using the space group $P\text{-}3c1$ and the approximate unit cell parameters $a=b=5.58$ Å, $c=13.66$ Å. Fig. 2 shows the SAED patterns from the main zone axes ([100]/[12−1], [12−1], [001], and [−110]) of $Sr_3Fe_2TeO_9$. The [100] and [12−1] SAED patterns overlap in the first frame as a consequence of twinning in nanodomains smaller than the smallest SAED aperture of the microscope. As a consequence, the [100] electron diffraction pattern could not be found separately. However, the [100] zone axis pattern can be seen in pure form as the Fourier transform of the [100] HAADF-STEM image in Fig. 3. The reflection conditions $0kl$: $l=2n$, $00l$: $l=2n$ (4-index system: $h\text{-}h0l$: $l=2n$, $000l$: $l=2n$) derived from the electron diffraction patterns and Fourier transform leave as the only possible extinction symbol $P\text{--}c$. This allows space groups $P3c$ and $P\text{-}3c$. $P3c$ is a subgroup of $P\text{-}3c$ and is achieved by eliminating the 2-fold axis lying along the [100] direction of $P\text{-}3c$. However, because of the inversion centre added in diffraction experiments, we cannot determine the presence or absence of this axis from SAED. Convergent beam electron diffraction would normally allow us to determine the presence of a two-fold axis, but this cannot be done for $Sr_3Fe_2TeO_9$ because of the twinning and presence of a second phase in the crystals, see below. Among the other maximal subgroups of $P\text{-}3c$, only $P2/c$ would correspond to the reflection conditions, but we see no experimental indication that the symmetry should be lowered to monoclinic. Therefore, the highest symmetry space group fitting all the experimental results has been used, which is $P\text{-}3c$ In the top left image in Fig. 3, taken along [100], horizontal rows of uniformly bright dots alternate with rows in which pairs of weak dots are separated from each other by one bright dot. In HAADF-STEM images, the brightness of the dots increases with the average atomic number, Z, of a projected column. Sr, Fe and Te have the atomic numbers 38, 26 and 52, respectively. The weakest dots thus correspond to columns of Fe, and the brightest to columns of Te; the homogeneously bright rows are populated by Sr. This assignment is confirmed by the high resolution EDX maps shown in Fig. 3. The contrast in the [001] image shown in Fig. 4 and the inserted atomic resolution EDX map also show evidence of cation order. Here the structure is viewed down columns in which Sr atoms alternate with octahedral sites; the 2:1 sequence of weak and strong dots in the lines of atoms running down the page clearly shows the presence of 2:1 Fe:Te ordering. Fig. 5 shows a [100] and a [001] view of a trigonal perovskite unit cell with this 2:1 ordering of Fe and Te over the octahedral sites. The observation of [100]/[12−1] twinning prompted the collection of more images, taken from more than one sample, in an attempt to assess the extent to which the microstructure is disrupted. These images showed that the [12−1] domains observed in what is essentially a [100] projection range in size from a few nanometers to ~50 nm in diameter, see Fig. S2. Furthermore, although the trigonal phase dominates the images, we observed crystallites that contained both trigonal regions and regions showing a checkerboard-like alternation of cations over the six-coordinate sites, see Fig. 6. The contrast variations in the latter regions match the variation of electron density in the tetragonal structural model described above, see Fig. 1. Therefore and for conciseness, in Fig. 6 these areas are labelled as $I4/m$. Note that the electron diffraction patterns labelled as the trigonal [12−1] zone in Fig. 2 could also be the [100] zone of the $I4/m$ phase as the two cannot be distinguished from their electron diffraction patterns alone. They can, however, be distinguished from their HAADF-STEM images, see Fig. 6.

In the light of the microscopy data presented above, the XRPD data were reanalysed in space group $P\text{-}3c1$ using the structural model shown in Fig. 5. The overall quality of the Rietveld fit achieved using this trigonal structure was essentially the same ($R_{wpr}=6.04\%$, $\chi^2=1.46$ see Fig. S2) as that achieved in tetragonal symmetry, with different weak reflections, for example at $2\theta=19°$, being unaccounted for. Consequently our final analysis treated the sample as a mixture of a trigonal phase and a tetragonal phase, the latter in space group $I4/m$. In the trigonal structure there are two independent oxygen sites (6$f$ and 12$g$), two A sites (2$a$ and 4$d$) that accommodate strontium atoms, and two independent B-sites (4$d$ and 2$b$) for iron and tellurium, see Table 1. In our refinements we assumed that the iron and tellurium cations are completely ordered over the latter two sites and thus the cation arrangement in the trigonal phase can be expressed as $Sr[Fe^{3+}_{0.6667}]_{(4d)}[Te^{6+}_{0.3333}]_{(2b)}O_3$. In the tetragonal structure, however, there is only one position (4$d$) for strontium, and the two distinct B-sites (2$a$ and 2$b$) have equal multiplicities. We assumed that one is fully occupied by iron and the other by a random distribution of iron (33%) and tellurium (67%) to give an overall 2:1 stoichiometry of iron and tellurium. In this case the cation arrangement can be described as $Sr[Fe^{3+}_{0.5}]_{(2a)}[Fe^{3+}_{0.1667}Te^{6+}_{0.3333}]_{(2b)}O_3$. This two-phase model, with the trigonal and tetragonal phases occurring in a ratio of 73.8(6):26.2(6), accounted for all the observed peaks. The agreement achieved between the observed and calculated diffraction patterns in this case ($R_{wpr}=5.93\%$, $\chi^2=1.41$) can be seen in Fig. 7.

$^{57}$Fe Mössbauer spectra collected from $Sr_3Fe_2TeO_9$ at room temperature are shown in Fig. 8. The low-resolution spectrum, see Fig. 8(a), clearly has a substantial magnetic component. From the shape of the lines in the magnetic sextet it is apparent that there is a distribution of magnetic hyperfine fields, rather than a single, well-defined field strength. This observation suggests that there might be slightly different nearest-neighbour environments around the iron sites. The higher-resolution, low velocity spectrum, see Fig. 8(b), shows that the central part of the spectrum contains at least two paramagnetic doublets in addition to the two innermost lines of the hyperfine sextet. Quantitative analysis of

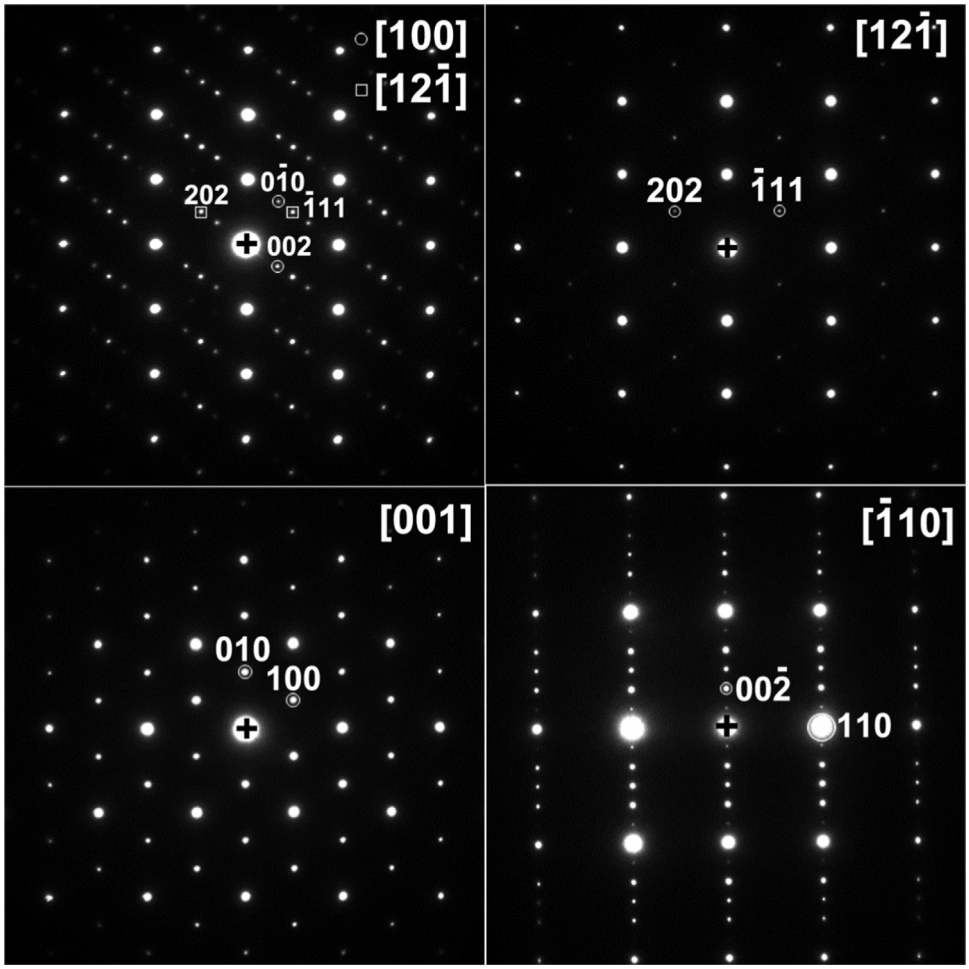


**Fig. 2.** Representative SAED patterns of the main zones of $Sr_3Fe_2TeO_9$.

this spectrum resulted in the parameters shown in Table 2. The tabulated spectral weights lead to the conclusion that ~41% of the total absorption is in the hyperfine sextet. Our fit to the spectrum shown in Fig. 8(a), obtained using the Le Caër–Dubois method, therefore included two quadrupole doublets and a hyperfine field distribution; the latter is shown in Fig. 9. The average hyperfine magnetic field obtained from the distribution is 43.1 T with a standard deviation of 4.1 T and the average isomer shift of the magnetic component is $+0.41(3)$ mm s$^{-1}$ relative to the centre of the α-Fe calibration spectrum. Although the degree of spectral overlap and the presence of a range of hyperfine fields make it difficult to obtain a unique description of the spectra, our analysis of the Mössbauer spectrum obtained on the extended velocity scale suggested that the magnetic component comprises ~36% of the spectrum, slightly lower than the value obtained by analysis of the central absorption alone. The two doublets that account for the remaining ~64% of the spectrum again have comparable spectral weights but significantly different quadrupole splittings, $|\Delta|$. In both analyses the isomer shifts of all components lie in the narrow range $0.27 \leq \delta/\text{mm s}^{-1} \leq 0.42$, suggesting that all the iron in $Sr_3Fe_2TeO_9$ is present as high-spin $Fe^{3+}$. The Mössbauer spectrum collected at 5 K is shown in Fig. S5. The central, paramagnetic absorption is no longer present and the hyperfine field has increased to ~52 T on cooling, although the width of the lines shows that a range of field strengths is again present. In view of the complexity of the system it was not possible to identify a unique set of physically-meaningful fitting parameters and so we did not pursue a more detailed, quantitative analysis of the Mössbauer spectra.

The neutron diffraction data collected at 300 K using wavelengths of 1.6220 and 2.4395 Å were analysed simultaneously in the same two-phase model used in the final analysis of the XRPD data. Refinement of the atomic coordinates and atomic displacement parameters associated with this model did not give an entirely satisfactory account of the data. The discrepancies between the observed and calculated diffraction profiles were most noticeable at low angles and were therefore assumed to be magnetic in origin. Furthermore, Ivanov et al. reported a value of 260 K for the magnetic transition temperature in tetragonal $Sr_3Fe_2TeO_9$ and it is therefore reasonable to assume that the magnetic scattering observed at 300 K is associated with the trigonal phase. However, in order to complete the analysis and deduce a detailed model for the magnetic structure it was necessary to consider the Mössbauer spectra described above. We assumed the two doublets to be of equal intensity and assigned one to each of the trigonal and tetragonal phases. If the hyperfine field is associated with the trigonal phase then, on the basis of the Le Caër–Dubois fit, $(36+32)=68\%$ of the sample is trigonal and 32% is tetragonal. A calculation based on the data in Table 2 gives a ratio of 70.5:29.5. Both of these ratios are in reasonable agreement with the ratio of ~74:26 deduced from the XRPD data and so we assumed that our partition of the absorption between the two phases was correct. Hence we deduced that 53–58% of the iron in the trigonal phase is magnetically ordered at room temperature. The antiferromagnetic structure shown in Fig. 10 gives rise to additional intensity in the Bragg peaks that were mis-fitted when magnetic scattering was neglected in our initial analysis of the neutron data. Each $Fe^{3+}$ cation is coupled antiferromagnetically to its neighbouring sites, whether

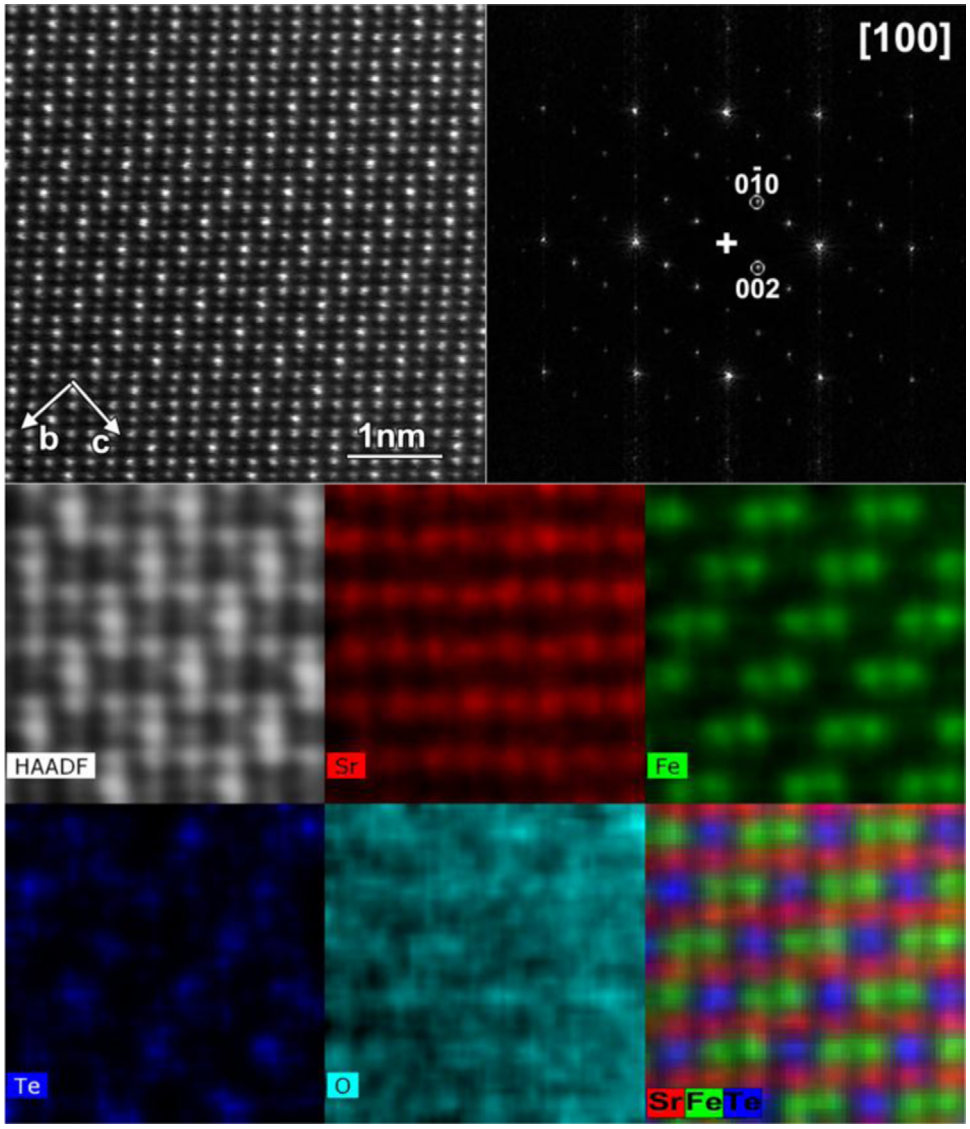


**Fig. 3.** Top: HAADF-STEM image of $Sr_3Fe_2TeO_9$ taken along the zone axis [100] and a Fourier transform of a pure [100] area. Bottom: HAADF-STEM image and corresponding atomic resolution EDX map of a [100] oriented area, showing the positions of the columns of Sr, Fe, Te and O atoms. (For colour-aided distinction between the Sr, Fe and Te atoms in this figure, the reader is referred to the web version of this article).

they are nearest neighbours or next-nearest neighbours that are separated by a $TeO_6$ octahedron. When 53% of the $Fe^{3+}$ ions in the trigonal phase were assumed to contribute to the magnetic scattering, the ordered magnetic moment refined to 3.60(5) $\mu_B$ per ordered cation; the calculated value of the moment is inversely proportional to the percentage of the $Fe^{3+}$ ions assumed to be ordered. A value of ~4.5 $\mu_B$ is expected in a defect-free, saturated antiferromagnet but the value of the hyperfine field is also lower than the value of ~55 T typically observed in that case and our model thus gives a reasonable and self-consistent account of the spectroscopic and diffraction data collected at room temperature. The inclusion of magnetic scattering in the Rietveld analysis resulted in agreement factors of $R_{wpr}$=4.67%, $\chi^2$=4.57. The concentration ratio of the trigonal and tetragonal phases refined to be 76:24, in agreement with the ratio determined by X-ray diffraction. The final observed and calculated diffraction profiles are shown in Fig. 11 and the refined structural parameters are listed in Table 1; the derived bond lengths and angles are listed in Table 3.

The observation of a hyperfine field of ~52 T at 5 K prompted us to assign a proportionately-enlarged magnetic moment to the ordered $Fe^{3+}$ cations in the trigonal phase during the analysis of the neutron diffraction data collected at 3 K. The tetragonal phase was again assumed to be non-magnetic; the validity of this assumption is discussed below. When the moment was held fixed at 4.34 $\mu_B$ per ordered cation, the value calculated from the hyperfine field, the fraction of magnetic $Fe^{3+}$ in the trigonal structure refined to be 55.6%, a value that lies within the range deduced from the room-temperature Mössbauer spectra. The refined structural parameters obtained at 3 K are listed in Table 4 and selected bond lengths are included in Table 3. The observed and calculated diffraction patterns are shown in Fig. S4.

The temperature dependence of the molar magnetic susceptibility of our sample of $Sr_3Fe_2TeO_9$ is shown in Fig. 12. The data collected under ZFC and FC conditions overlie at high temperatures but the ZFC susceptibility has a maximum at 80 K whereas the FC susceptibility has a negative temperature gradient throughout the measured temperature range. The field dependence of the molar magnetisation is shown in Fig. 13. M(H) is linear at 300 K and no hysteresis is observed. At 150 K M(H) is no longer linear but hysteresis is only observed in the data collected at 5 K; the function is not symmetrical about the origin.

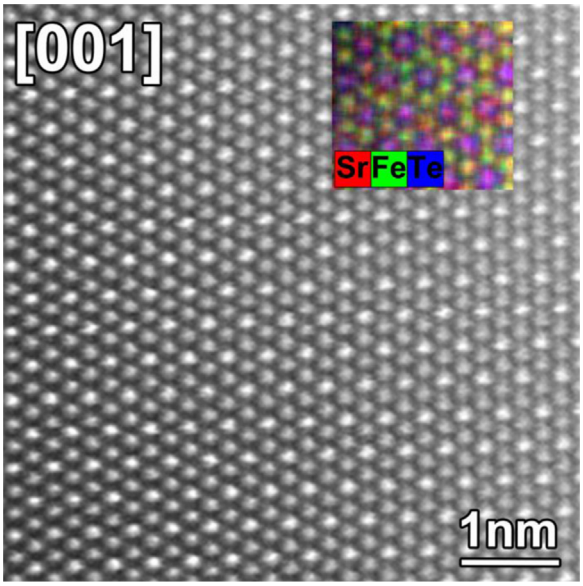


**Fig. 4.** HAADF-STEM image of $Sr_3Fe_2TeO_9$ taken along the [001] zone axis. The inset is an atomic resolution EDX map showing the positions of the different cations along this projection. There is an overlap of A and B cations along this projection. (For colour-aided distinction between the Sr, Fe and Te atoms in this figure, the reader is referred to the web version of this article).

## 4. Discussion

It is clear that our sample of $Sr_3Fe_2TeO_9$ differs from those prepared by Djerdi et al., Ivanov et al. and Augsburger et al., and that their samples are different from each other. This is most clearly shown by a comparison of the temperature dependence of the magnetic susceptibility measured in each case and, in the case of Augsburger et al., by a comparison of the X-ray diffraction patterns. The most obvious differences between our synthesis and those performed by Ivanov et al. and Augsburger et al. lie in the use of telluric acid, rather than $TeO_2$, by Augsburger et al. and of SrO, rather than $SrCO_3$, by Ivanov et al. Furthermore, both of these groups used an annealing temperature of only 950 °C. Our choice of 1200 °C was made when heating the reactants at 950 °C failed to produce a perovskite-like phase. The sol-gel protocol used by Djerdi et al. ended with an anneal at 1300 °C. Their cubic sample differs most markedly from our own in terms of both crystal structure and physical properties. For example, although magnetic order is present in our sample at 300 K, there is no evidence of a spontaneous magnetisation at that temperature.

Our initial attempts to analyse our X-ray diffraction pattern were influenced by our awareness of the earlier studies of this compound and our apparent success in accounting for the data using a monophasic model in tetragonal symmetry will make us more cautious in the future. The results of our electron-microscopy study demonstrated that our approach was flawed and they also revealed the full complexity of the system. The electron diffraction patterns, see Fig. 2, indicated that the sample has trigonal symmetry and the HAADF-STEM images and EDX maps shown in Figs. 3 and 4 reveal the presence of the 2:1 Fe:Te ordering pattern shown in Fig. 5. This type of cation ordering over the B sites of a perovskite is relatively unusual, with many $A_3B_2B'O_9$ compositions, for example $La_3Ni_2SbO_9$, adopting the 1:1 ordering pattern illustrated in Fig. 1, even though the trigonal pattern might be considered a better match for their stoichiometry. Although there are some exceptions, for example $Ba_3Bi_2TeO_9$ [17], the latter pattern is most commonly observed in $A_3^{2+}B_2^{5+}B'^{2+}O_9$ compounds [18,19]. Like $Sr_3Fe_2TeO_9$, these compounds have only divalent cations on the A site and two types of cation with a charge difference of +3

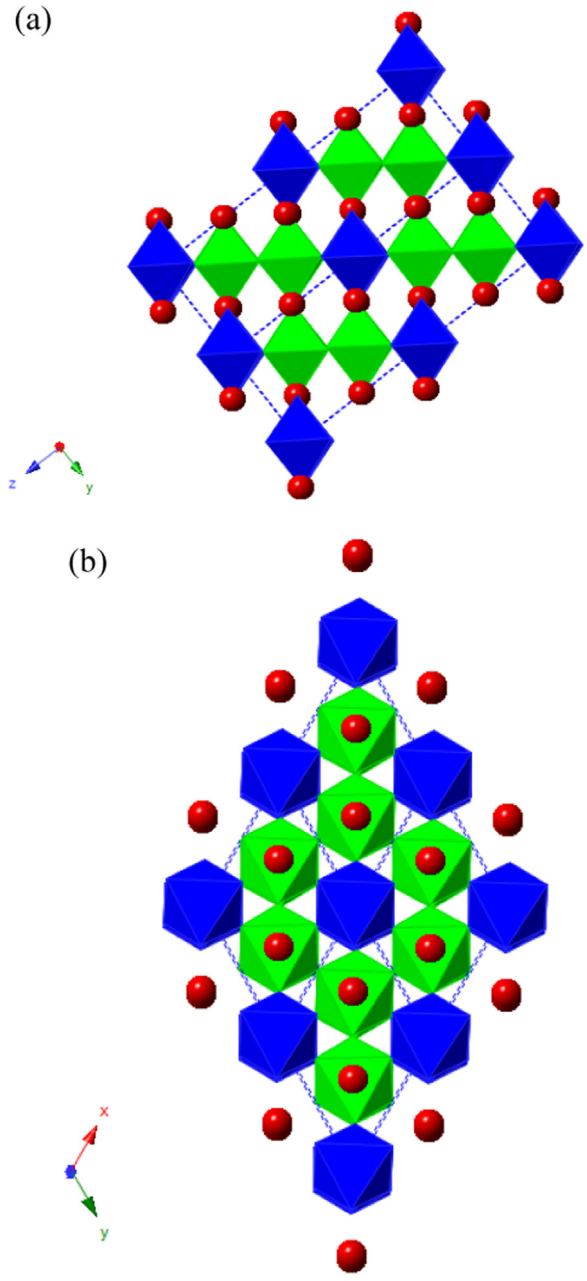


**Fig. 5.** Polyhedral representation of the crystal structure of $Sr_3Fe_2TeO_9$ in the trigonal space group *P*-3*c*1 viewed along (a) [100] and (b) [001]; $FeO_6$ and $TeO_6$ octahedra are shown in green and blue, respectively. Red circles represent the $Sr^{2+}$ cations. (For interpretation of the references to color in this figure legend, the reader is referred to the web version of this article).

on the octahedral sites. $Sr_3CaRu_2O_9$ and the high-pressure forms of $Ba_3CaRu_2O_9$ and $Ba_3CaIr_2O_9$ are the only such compounds wherein the majority six-coordinate cation is paramagnetic [20–22]. The high-pressure phase of $Ba_3NaRu_2O_9$ has a different charge distribution over the octahedral sites but also adopts the 2:1 ordered structure [23]. We note that $Ba_3Fe_2TeO_9$ is a 6H hexagonal perovskite [7,9] because, in the absence of the large $Bi^{3+}$ cation, the cation size ratio $r_A/r_B$ is too large to stabilise a pseudo-cubic perovskite structure.

Our microscopy study revealed that defects are present in the structure of $Sr_3Fe_2TeO_9$. More specifically, the electron diffraction patterns indicated that twinning was present on the nanoscale in some of the crystallites studied and the HAADF-STEM images showed that, in addition to the dominant 2:1 cation ordering,

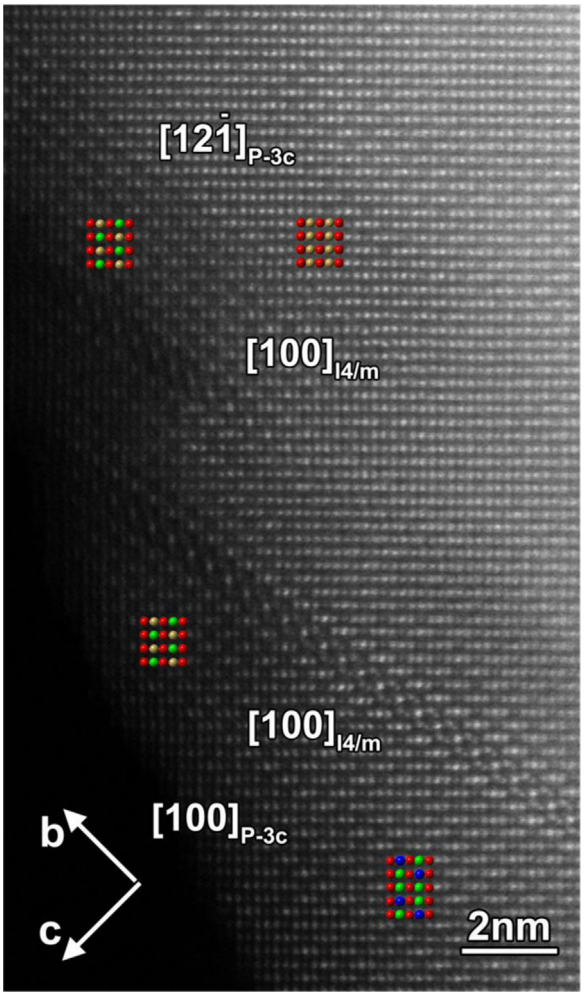


**Fig. 6.** HAADF STEM image of $Sr_3Fe_2TeO_9$ showing the coexistence of areas with chessboard order (labelled *I*4/*m* [100]), *P*-3*c* [100] and *P*-3*c* [12−1]. The colour overlays clarify the order of the atoms in the surrounding areas; Sr, Fe and Te are red, green and blue respectively. Khaki represents columns with, in this projection, a mix of Fe and Te. (For interpretation of the references to color in this figure legend, the reader is referred to the web version of this article).

**Table 1**
Atomic parameters of $Sr_3Fe_2TeO_9$, refined from neutron diffraction data collected at 300 K.

| Atom | Site | *x* | *y* | *z* | $U_{iso}$ | Fractional occupancy |
|---|---|---|---|---|---|---|
| *Phase 1* | | | | | | |
| Sr1 | 2*a* | 0 | 0 | 0.25 | 0.005(1) | 1.0 |
| Sr2 | 4*d* | 0.6667 | 0.3333 | 0.5834(6) | 0.0088(6) | 1.0 |
| Fe | 4*d* | 0.6667 | 0.3333 | 0.3335(5) | 0.0036(3) | 1.0 |
| Te | 2*b* | 0 | 0 | 0 | 0.0036(3) | 1.0 |
| O1 | 6*f* | 0.521(1) | 0 | 0.25 | 0.014(1) | 1.0 |
| O2 | 12*g* | 0.1942(6) | 0.3308(8) | 0.5842(4) | 0.0062(5) | 1.0 |
| *Phase 2* | | | | | | |
| Sr | 4*d* | 0 | 0.5 | 0.25 | 0.026(1) | 1.0 |
| Fe1 | 2*a* | 0 | 0 | 0 | 0.023(4) | 1.0 |
| Fe2 | 2*b* | 0 | 0 | 0.5 | 0.003(3) | 0.3333 |
| Te | 2*b* | 0 | 0 | 0.5 | 0.003(3) | 0.6667 |
| O1 | 4*e* | 0 | 0 | 0.242(6) | 0.024(3) | 1.0 |
| O2 | 8*h* | 0.285(3) | 0.217(2) | 0 | 0.021(1) | 1.0 |

$R_{wp}$=4.67%, $R_p$=3.56%, $\chi^2$=4.568.
Phase 1: space group *P* -3*c*1, a=5.5761(3) Å, c=13.654(1) Å, weight fraction=76%.
Phase 2: space group *I* 4/*m*, a=5.5886(5) Å, c=7.9134(8) Å, weight fraction=24%.
Cell transformation: $\mathbf{a}_1=0.5(-\mathbf{a}_2-\mathbf{b}_2+\mathbf{c}_2)$; $\mathbf{b}_1=\mathbf{a}_2$; $\mathbf{c}_1=2\mathbf{b}_2+\mathbf{c}_2$.

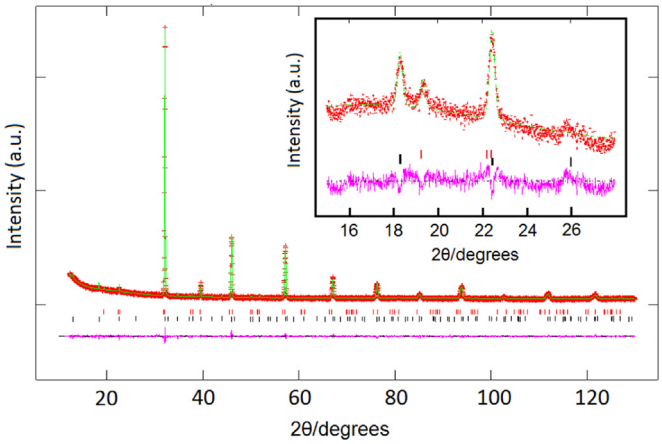


**Fig. 7.** Observed (red crosses) and calculated (green line) X-ray powder diffraction patterns for $Sr_3Fe_2TeO_9$ sample; a difference curve (purple) is shown. Black (red) vertical bars represent the positions of Bragg reflection for the trigonal (tetragonal) phase. The inset shows the low-angle region of a pattern collected in high-intensity mode in order to emphasise the most important weak reflections. (For interpretation of the references to color in this figure legend, the reader is referred to the web version of this article).

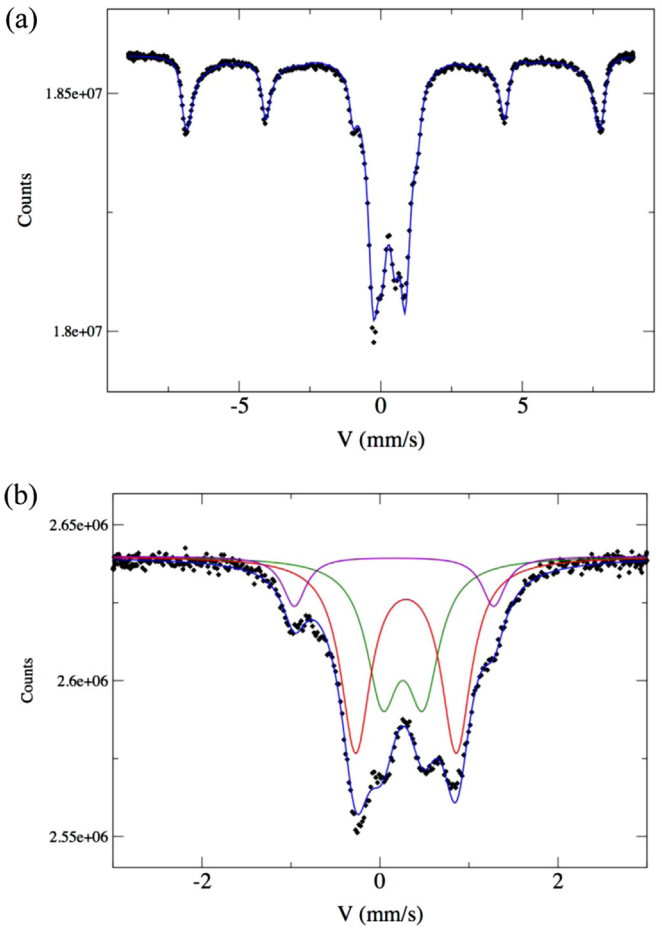


**Fig. 8.** (a) $^{57}$Fe Mössbauer spectrum of $Sr_3Fe_2TeO_9$ obtained at room temperature (295 K) on an extended velocity scale. The fitted curve employed a distribution of hyperfine field, as described in the text. (b) $^{57}$Fe Mössbauer spectrum of $Sr_3Fe_2TeO_9$ obtained at room temperature (295 K) on a reduced velocity scale.

some crystallites had regions where 1:1 ordering was present, see Fig. 6. This ordering is consistent with the tetragonal structure proposed by Ivanov et al., but also with the monoclinic structure of $La_3Ni_2SbO_9$ [10]. Our data do not allow us to distinguish

**Table 2**
$^{57}$Fe Mössbauer hyperfine parameters of $Sr_3Fe_2TeO_9$, obtained by fitting the spectrum shown in Fig. 8(b). The errors are estimates.

| Isomer shift (δ mm/s) ± 0.02 mm/s | Quadrupole splitting (\| Δ\| mm/s) ± 0.03 mm/s | % Area ± 1.5% |
|---|---|---|
| 0.37 | 0.49 | 43.2 |
| 0.41 | 1.15 | 46.4 |
| 0.27 | 2.23 | 10.4 ('sextet' contribution) |

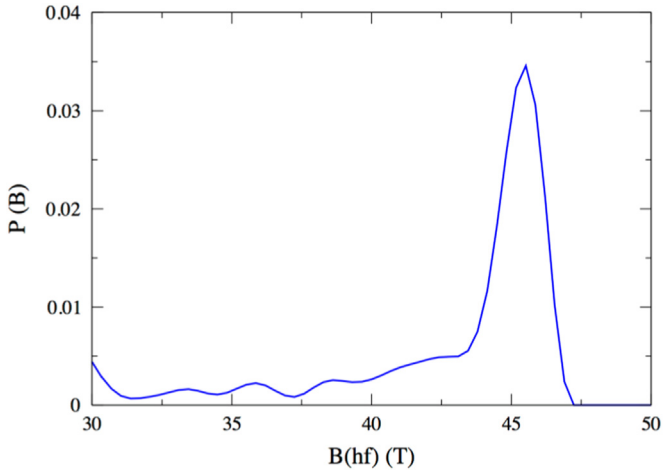


**Fig. 9.** The distribution of hyperfine magnetic field obtained from the fit to the room temperature Mössbauer spectrum of $Sr_3Fe_2TeO_9$.

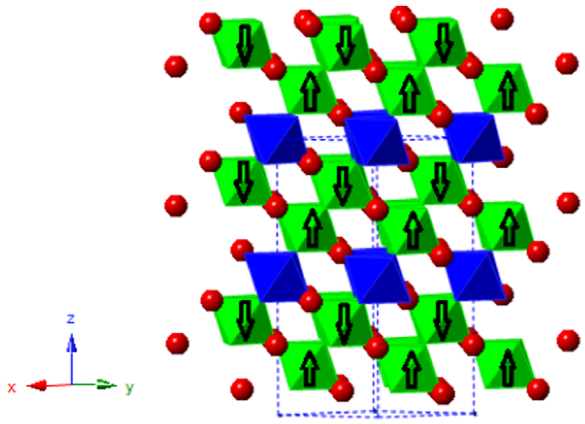


**Fig. 10.** Magnetic structure of the trigonal phase of $Sr_3Fe_2TeO_9$. Green and blue octahedra represent $Fe^{3+}$ and $Te^{6+}$ sites, respectively, and red circles represent $Sr^{2+}$ cations. Black arrows represent the ordered magnetic moments of the $Fe^{3+}$ cations. (For interpretation of the references to color in this figure legend, the reader is referred to the web version of this article).

unambiguously between the two symmetries so, in the light of the previous studies of this compound, we assumed these regions to be tetragonal. We were able to optimise the fit to our XRPD pattern when we included a trigonal phase and a minority tetragonal phase, thus demonstrating that some of the 1:1 ordered regions are large enough to give rise to Bragg peaks. Given that our mixed trigonal/tetragonal sample was prepared at a higher temperature than the tetragonal sample described by Ivanov et al., we carried out further syntheses with week-long anneals at 950 and 1200 °C in an attempt to prepare monophasic tetragonal and trigonal samples, respectively. The resulting XRPD patterns always showed the presence of both phases, with a trigonal: tetragonal ratio that varied between 70:30 and 80:20.

The agreement between the observed and calculated neutron

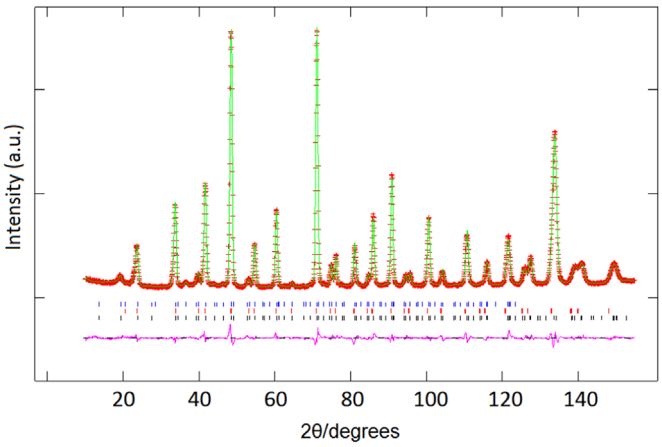


**Fig. 11.** Observed (red crosses) and calculated (green line) neutron diffraction patterns for $Sr_3Fe_2TeO_9$ at 300 K; a difference curve (purple) is shown. Black, red and blue vertical bars represent the positions of Bragg reflections for the trigonal, tetragonal and magnetic phases, respectively. λ = 1.6215 Å. (For interpretation of the references to color in this figure legend, the reader is referred to the web version of this article).

**Table 3**
Selected interatomic distances (Å) and bond angles (degrees) in $Sr_3Fe_2TeO_9$ at 300 K and 3 K.

| | 300 K | 3 K |
|---|---|---|
| Trigonal phase, space group *P* -3*c*1 | | |
| Sr1–O1 | 2.673(6) × 3 | 2.581(7) × 3 |
| Sr1–O1 | 2.903(6) × 3 | 2.982(7) × 3 |
| Sr1–O2 | 2.776(5) × 6 | 2.781(6) × 6 |
| Sr2–O1 | 2.790(7) × 3 | 2.798(8) × 3 |
| Sr2–O2 | 2.627(3) × 3 | 2.618(4) × 3 |
| Sr2–O2 | 2.949(3) × 3 | 2.945(4) × 3 |
| Sr2–O2 | 2.809(8) × 3 | 2.78(1) × 3 |
| Fe–O1 | 1.976(4) × 3 | 1.974(4) × 3 |
| Fe–O2 | 1.980(5) × 3 | 1.991(7) × 3 |
| Te–O2 | 1.974(5) × 6 | 1.958(6) × 6 |
| O1–Fe –O1 | 90.1(2) | 90.4(2) |
| O2–Fe–O2 | 90.9(3) | 90.3(4) |
| O1–Fe–O2 | 178.6(3) | 178.9(3) |
| | 88.6(2) | 88.9(2) |
| | 90.4(2) | 90.3(4) |
| Tetragonal phase, space group *I* 4/*m* | | |
| Sr–O1 | 2.795(1) × 4 | 2.7908(5) × 4 |
| Sr–O2 | 2.991(4) × 4 | 2.988(3) × 4 |
| Sr–O2 | 2.614(4) × 4 | 2.611(2) × 4 |
| Fe1–O1 | 1.92(5) × 2 | 2.02(3) × 2 |
| Fe1–O2 | 1.98(2) × 4 | 2.05(2) × 4 |
| Fe2/Te–O1 | 2.04(5) × 2 | 1.94(3) × 2 |
| Fe2/Te–O2 | 2.01(2) × 4 | 1.93(2) × 4 |

diffraction profiles shown in Fig. 11 is good. The Fe–O and Te–O bond lengths determined by neutron diffraction, see Table 3, are essentially equal in the trigonal phase at 300 K but the Te–O bond is shorter, as expected [24] at 5 K. The difference in bond lengths around the two, six-coordinate sites is apparently more marked in the minority tetragonal phase, although these distances are less precisely determined. In addition to the quality of the fit, two additional pieces of evidence show that the magnetic hyperfine splitting observed in the Mössbauer spectra collected at room temperature is associated with the trigonal phase. Firstly, the fraction of the total absorption contained in the sextet is too large to derive from the iron in the minority tetragonal phase and, secondly, neutron diffraction data collected at room temperature by Ivanov et al. showed no evidence of magnetic ordering. We put more weight on their data than those of Augsburger et al. because the latter draw attention to the presence of one impurity, albeit

**Table 4**
Atomic parameters of $Sr_3Fe_2TeO_9$, refined from neutron diffraction data collected at 3 K.

| Atom | Site | *x* | *y* | *z* | $U_{iso}$ | Fractional occupancy |
|---|---|---|---|---|---|---|
| *Phase 1* | | | | | | |
| Sr1 | 2*a* | 0 | 0 | 0.25 | 0.0003(14) | 1.0 |
| Sr2 | 4*d* | 0.6667 | 0.3333 | 0.5824(7) | 0.0041(7) | 1.0 |
| Fe | 4*d* | 0.6667 | 0.3333 | 0.3330(5) | 0.0025(2) | 1.0 |
| Te | 2*b* | 0 | 0 | 0 | 0.0025(2) | 1.0 |
| O1 | 6*f* | 0.536(1) | 0 | 0.25 | 0.003(1) | 1.0 |
| O2 | 12*g* | 0.1944(8) | 0.330(1) | 0.5830(5) | 0.0058(7) | 1.0 |
| *Phase 2* | | | | | | |
| Sr | 4*d* | 0 | 0.5 | 0.25 | 0.0156(8) | 1.0 |
| Fe1 | 2*a* | 0 | 0 | 0 | 0.0037(6) | 1.0 |
| Fe2 | 2*b* | 0 | 0 | 0.5 | 0.0037(6) | 0.3333 |
| Te | 2*b* | 0 | 0 | 0.5 | 0.0037(6) | 0.6667 |
| O1 | 4*e* | 0 | 0 | 0.255(4) | 0.0087(6) | 1.0 |
| O2 | 8*h* | 0.291(2) | 0.223(2) | 0 | 0.0087(6) | 1.0 |

$R_{wp}$=6.23%, $R_p$=4 0.69%, $\chi^2$=8.033.
Phase 1: space group *P* -3*c*1, a=5.5626(3) Å, c=13.622(1) Å, weight fraction=76%.
Phase 2: space group *I* 4/*m*, a=5.5810(4) Å, c=7.9045(7) Å, weight fraction=24%.

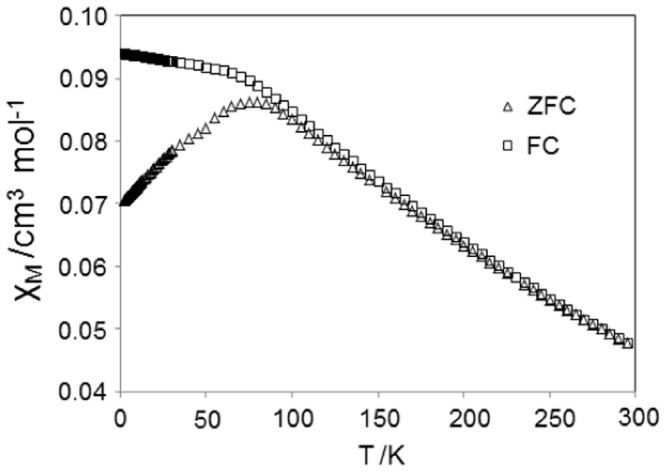


**Fig. 12.** Temperature dependence of the molar magnetic susceptibility of $Sr_3Fe_2TeO_9$.

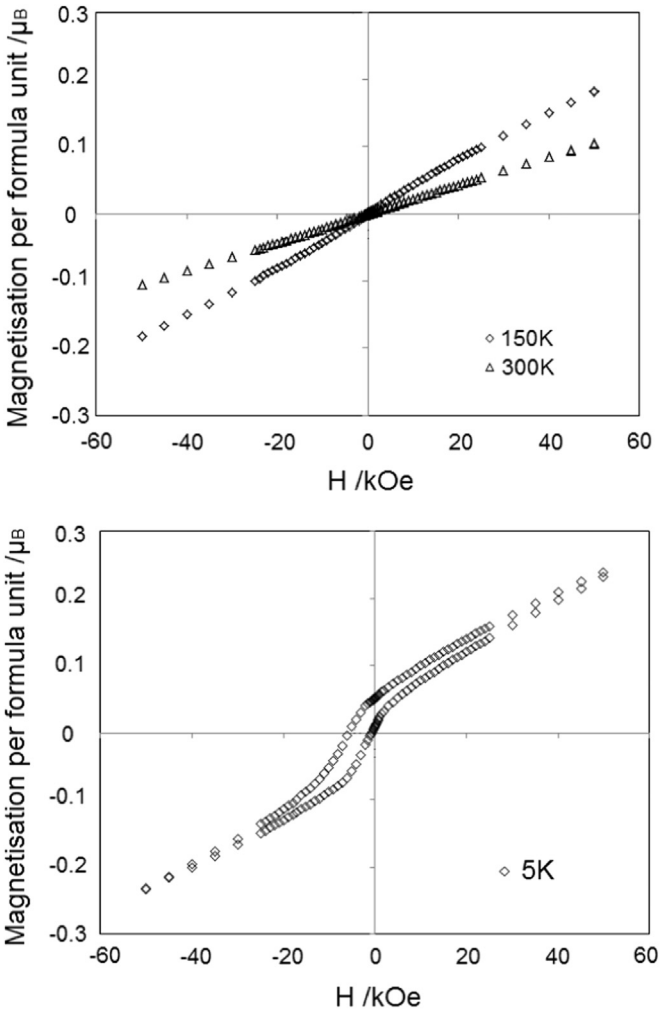


**Fig. 13.** Field dependence of the molar magnetisation of $Sr_3Fe_2TeO_9$ at (a) 300 and 150 K and (b) 5 K.

diamagnetic, in their sample and we believe that the near-coincidence of the magnetic ordering temperatures of their $Ba_3Fe_2TeO_9$ and $Sr_3Fe_2TeO_9$ samples suggests that the same magnetic impurity might be present in both. With this assignment, the phase fractions derived from the diffraction and spectroscopic data are essentially self-consistent. It appears that some, but not all, of the $Fe^{3+}$ cations in the trigonal phase are antiferromagnetically ordered at room temperature. We attribute the range of observed hyperfine fields, see Fig. 9, and the incomplete ordering to the presence of the defects described above and illustrated in Fig. 6. The spectrum collected at 5 K shows an increased magnetisation but when the atomic moment measured by neutron diffraction was fixed to be consistent with the internal hyperfine field there was no evidence to suggest that significantly more spins join the antiferromagnetic phase on cooling below room temperature. The absence of a paramagnetic component in the spectrum collected at 5 K demonstrates that all the spins in the sample are either ordered or frozen in a spin glass at that temperature. Unlike Ivanov et al. we see no evidence for a magnetic transition in the tetragonal phase at 260 K, see Fig. 12, and hysteresis is clearly present in $\chi$(T) below 80 K. We therefore suggest that all the spins that are disordered at room temperature undergo a transition to a spin-glass state on cooling below 80 K. If the tetragonal regions in our sample were to adopt a long-range ordered structure with atomic moments as small as those reported by Ivanov et al., then the combination of the low phase-fraction and the weak moments would prevent it from being detected in the neutron diffraction data collected at 3 K. However, there is no evidence in the low-temperature Mössbauer spectrum for a component with a weak internal hyperfine field and there is no evidence in the neutron data for a second magnetic component with a strong moment, see Fig. 11. The participation of the tetragonal regions in the spin-glass transition is thus consistent with all the available data. The magnetic structure shown in Fig. 10 satisfies what must be the very strong superexchange interactions between $Fe^{3+}$ cations in neighbouring, corner-sharing octahedra. We cannot offer a detailed discussion of the magnitudes of the ordered magnetic moments because of the correlations between the fraction of the total iron in the ordered phase and the magnitude of the moment. We believe this to be the first observation of long-range magnetic ordering in a trigonal 2:1 cation-ordered perovskite.

The behaviour of M(H) shown in Fig. 13 is consistent with our model. The absence of hysteresis at 300 K confirms that the magnetic Bragg scattering observed in the neutron diffraction pattern comes from a phase that is antiferromagnetic, rather than ferrimagnetic or ferromagnetic. The non-linearity of the function at 150 K suggests that significant, intercation interactions are present, as is to be expected at this temperature in an oxide rich in $Fe^{3+}$ cations, and the shifted hysteresis loop recorded at 5 K is

typical of a spin glass. The observation of this type of behaviour in pseudo-cubic perovskites with a partially ordered distribution of equal numbers of two cation species has been seen previously and attributed to the competition between nearest–neighbour and next–nearest–neighbour interactions [25,26]. In the case of the minority phase in $Sr_3Fe_2TeO_9$, the small domain size is also likely to be a factor.

## 5. Conclusions

$Sr_3Fe_2TeO_9$ is a complex material. The structure and properties are clearly sensitive to the synthesis conditions. We have shown for the first time that the compound, when synthesised at 1200 °C, adopts a trigonal perovskite-like structure with the $Fe^{3+}$ and $Te^{6+}$ cations ordering in a 2:1 sequence that is compatible with both the chemical composition and the multiplicities of the crystallographically distinct six-coordinate sites in the trigonal space group. This is not the case in many other $A_3B_2B'O_9$ compounds, including the relaxor ferromagnet $La_3Ni_2SbO_9$. The difference in the cation ordering pattern is the most likely reason that the magnetic behaviour of the two compounds differs so markedly, with the trigonal phase of $Sr_3Fe_2TeO_9$ being antiferromagnetic at room temperature. However, the trigonal structure is disrupted by both nano-twinning and regions where the cations order in a 1:1 sequence. These disruptions prevent full antiferromagnetic ordering throughout the sample and the unordered spins form a spin-glass phase that coexists with the antiferromagnetic phase below 80 K.

## Acknowledgements

PDB, RPS and JH thank the SCG and EPSRC for financial support, the latter through Grant EP/M018954/1. JMC is grateful to G.A. Stewart for the use of his cryostat.

## Appendix A. Supplementary material

Supplementary data associated with this article can be found in the online version at http://dx.doi.org/10.1016/j.jssc.2016.06.024.

## References

[1] S.A. Bhalla, R. Guo, R. Roy, Mater. Res. Innov. 4 (2000) 3–26.
[2] R. Rodriguez, A. Fernandez, A. Isalgue, J. Rodriguez, A. Labarta, J. Tejada, X. Obradors, J. Phys. C: Solid State Phys. 18 (1985) L401.
[3] A. Callaghan, C.W. Moeller, R. Ward, Inorg. Chem. 5 (1966) 1572.
[4] S.W. Cheong, M. Mostovoy, Nat. Mater. 6 (2007) 13–20.
[5] M.T. Anderson, K.B. Greenwood, G.A. Taylor, K.R. Poeppelmeier, Progress Solid State Chem. 22 (1993) 197.
[6] S. Vasala, M. Karppinen, Progress Solid State Chem. 43 (2015) 1–36.
[7] M.S. Augsburger, M.C. Viola, J.C. Pedregosa, R.E. Carbonio, J.A. Alonso, J. Mater. Chem. 16 (2006) 4235–4242.
[8] S.A. Ivanov, P. Nordblad, S.G. Eriksson, R. Tellgren, H. Rundlof, Mater. Res. Bull. 42 (2007) 776–789.
[9] I. Djerdj, J. Popović, S. Mal, T. Weller, M. Nuskol, Z. Jagličić, Ž. Skoko, D. Pajić, C. Suchomski, P. Voepel, R. Marschall, B. Kozlevčar, B.M. Smarsly, Cryst. Growth Des. (2016).
[10] P.D. Battle, S.I. Evers, E.C. Hunter, M. Westwood, Inorg. Chem. 52 (2013) 6648.
[11] P.D. Battle, M. Avdeev, J. Hadermann, J. Solid State Chem. 220 (2014) 163.
[12] A.C. Larson, R.B. Von Dreele, General Structure Analysis System (GSAS), Los Alamos National Laboratory Report LAUR 2004, pp. 86–748.
[13] H.M. Rietveld, J. Appl. Crystallogr. 2 (1969) 65.
[14] B. v anLaar, W.B. Yelon, J. Appl. Cryst. 17 (1984) 47–54.
[15] R.A. Brand, ⟨http://www.wissel-instruments.de/⟩.
[16] G. Le Caër, J.M. Dubois, J. Phys. E-Sci. Instrum. 12 (1979) 1083–1090.
[17] J.H. Park, P.M. Woodward, Int. J. Inorg. Mater. 2 (2000) 153–166.
[18] P.K. Davies, H. Wu, A.Y. Borisevich, I.E. Molodetsky, L. Farber, Annu. Rev. Mater. Res. (2008) 369–401.
[19] U. Treiber, S. Kemmlersack, J. Solid State Chem. 43 (1982) 51–62.
[20] J.T. Rijssenbeek, S. Malo, V. Caignaert, K.R. Poeppelmeier, J. Am. Chem. Soc. 124 (2002) 2090–2091.
[21] J.T. Rijssenbeek, T. Saito, S. Malo, A.T. Masaki, M. Takano, K.R. Poeppelmeier, J. Am. Chem. Soc. 127 (2005) 675–681.
[22] J.G. Zhao, L.X. Yang, Y. Yu, F.Y. Li, R.C. Yu, C.Q. Jin, J. Solid State Chem. 182 (2009) 327–330.
[23] A.M. Arevalo-Lopez, M.S. Senn, L. Skedd, J.P. Attfield, Z. Anorg. Allg. Chem. 640 (2014) 1164–1167.
[24] R.D. Shannon, Acta Crystallogr. A 32 (1976) 519.
[25] P.D. Battle, T.C. Gibb, A.J. Herod, S.-H. Kim, P.H. Munns, J. Mater. Chem. 5 (1995) 865.
[26] P.D. Battle, T.C. Gibb, A.J. Herold, J.P. Hodges, J. Mater. Chem. 5 (1995) 75.